Journal of Materials Chemistry C

Two-Dimensional Solid-Phase Crystallization toward Centimeter-Scale Monocrystalline Layered $MoTe_2$ via Two-Step Annealing

Journal:	*Journal of Materials Chemistry C*
Manuscript ID	TC-ART-07-2021-003123.R1
Article Type:	Paper
Date Submitted by the Author:	08-Oct-2021
Complete List of Authors:	Lin, Chih-Pin; National Yang Ming Chiao Tung University, Electronics Engineering Hsu, Hao-Hua; National Yang Ming Chiao Tung University, Electronics Engineering Huang, Jyun-Hong; National Yang Ming Chiao Tung University, Electronics Engineering Kang, Yu-Wei; National Yang Ming Chiao Tung University, Electronics Engineering Wu, Chien-Ting; Taiwan Semiconductor Research Institute Lee, Yao-Jen; Taiwan Semiconductor Research Institute Cheng, Chun-Cheng; AU Optronics Corporation, Lan, YannWen; National Taiwan Normal University, Department of physics Chang, Wenhao; National Yang Ming Chiao Tung University, Department of Electrophysics Li, Lain-Jong; University of Hong Kong, Hou, Tuo-Hung; National Yang Ming Chiao Tung University, Electronics Engineering

Two-Dimensional Solid-Phase Crystallization toward Centimeter-Scale Monocrystalline Layered $MoTe_2$ via Two-Step Annealing

Chih-Pin Lin, [a] *Hao-Hua Hsu,* [a] *Jyun-Hong Huang,* [a] *Yu-Wei Kang,* [a] *Chien-Ting Wu,* [b] *Yao-Jen Lee,* [b] *Chun-Cheng Cheng,* [c] *Yann-Wen Lan,* [d] *Wen-Hao Chang,* [e] *Lain-Jong Li,* [f] *and Tuo-Hung Hou* [*a]

[a]Department of Electronics Engineering and Institute of Electronics, National Yang Ming Chiao Tung University, Hsinchu 300, Taiwan

[b]Taiwan Semiconductor Research Institute, Hsinchu 300, Taiwan

[c]Advanced Technology Research Center, AU Optronics Corporation, Hsinchu 300, Taiwan

[d]Department of Physics, National Taiwan Normal University, Taipei 116, Taiwan

[e]Department of Electrophysics, National Yang Ming Chiao Tung University, Hsinchu 300, Taiwan

[f]Department of Mechanical Engineering, The University of Hong Kong, Pokfulam, Hong Kong SAR, China

[*]Electronic mail: thhou@mail.nctu.edu.tw

Abstract

The lack of effective synthesis techniques for achieving wafer-scale uniformity and high crystallinity remains one of the major obstacles for two-dimensional (2D) layered materials in practical applications. 2D solid-phase crystallization (2DSPC) is proposed based on the area-scalable and semiconductor-process-compatible sputtering and thermal annealing techniques. It successfully synthesizes few-layer 2H-$MoTe_2$ with a monocrystalline grain size exceeding half a centimeter on an amorphous substrate of silicon dioxide. The extremely large grain size is made possible through a two-step annealing process in inert ambient. The initial rapid thermal annealing at high temperatures produces hexagonal monocrystalline 2H-$MoTe_2$ seeds with low density and the subsequent long-duration furnace annealing at low temperatures enlarges the monocrystalline domains only from the preexisting seeds. The 2DSPC mechanism and its morphological evolution

agree with the classical nucleation theory and kinetic Wulff construction theory, respectively. Our result suggests the promising potential of 2DSPC as a simple yet effective route for synthesizing future wafer-scale, high-quality 2D materials.

Introduction

Two-dimensional (2D) layered materials, especially 2D semiconducting transition metal dichalcogenides (TMDs), such as MoS_2, $MoSe_2$, $MoTe_2$, WS_2, WSe_2, etc., are considered as the promising channel materials for the sub-3nm transistor technology because of their atomic thickness,[1,2] tunable bandgap,[3,4] high mobility,[5,6] and dangling-bond-free surface.[7,8] The 2D-TMD transistors demonstrated remarkable performance using the atomically thin channel,[9] and thus are now subject to active research in the semiconductor industry as the ultimate platform for scaled transistors.[10] Among various TMDs, research interests in $MoTe_2$ is growing rapidly owing to its intriguing properties of adequate bandgap (~1.1 eV),[11] high carrier mobility (~2500 cm^2/Vs),[12] large spin-orbit-coupling splitting (238 meV in valence band),[13] and tunable polymorphic semiconducting 2H and metallic 1T' phases (small 2H-1T' transformation energy barrier of ~40 meV per unit cell).[14] These distinctive characteristics could potentially enable many new applications in nanoelectronics, spintronics, and optoelectronics. Despite its promises, the lack of large-area and high-quality synthesis techniques remains one of the major obstacles for practical applications, which is true not only for $MoTe_2$ but also for 2D TMDs in general. The existence of numerous grain boundaries as a result of inferior crystallinity plays a vital role in the performance of 2D-based devices.[15,16] A general material synthesis strategy with wafer-scale uniformity, excellent film quality, and large grain size is critical for the future development of 2D electronics.

The grain size of each 2D material derived from different synthesis routes was summarized by A. Zavabeti et al.[17] Among various techniques, chemical vapor deposition (CVD) through chemical reactions of gaseous precursors is considered promising for synthesizing high-quality 2D layered TMDs with a large grain size at low cost.[18,19] For example, the monocrystalline domain of $MoSe_2$ synthesized by the ambient pressure CVD system was up to 2 mm.[20] S.-Y. Kim et al. further reviewed the recent advances of CVD in growing atomically thin MoS_2 layer in terms of precursor selection, growth temperature, substrate type, grain size, etc.[21] Most CVD methods produced grain sizes greater than 300 μm by sulfurizing a solid source (e.g. MoO_3) at high temperatures (>700 °C). Such vapor-phase growth technique, however, involves complicated precursor tuning (vapor

pressure, melting/reaction temperature, etc.) and process control (source-substrate configuration, turbulent flow, pressure, etc.). Therefore, achieving wafer-scale uniformity in film thickness, i.e. well-defined number of layers, for standard semiconductor production remains elusive. This is particularly challenging for Te-based TMDs where the critical size for indefinite vertical growth is relatively low, thus favoring vertically stacking with a non-uniform film thickness.[22] Recently, the step-edge epitaxy using the optimized CVD process was proposed as a promising strategy for synthesizing the large-grain 2D materials.[23] However, it remains challenging to guarantee flawless stitching between domains grown from a large number of orientation-aligned seeds even by using single-crystalline substrates. Furthermore, one such technique generally requires an additional transfer process to transfer 2D TMDs from the growth substrate to another insulating substrate for subsequent device fabrications, thus increasing the complexity in industrial applications. Therefore, wafer-level monocrystalline 2D TMDs directly grown on insulating substrates (e.g. SiO_2, Al_2O_3, HfO_2, etc.) are highly desirable. Recently, we demonstrated a simple yet effective route for synthesizing large-area, high-quality 2D-layered TMD films (e.g. MoS_2, $MoTe_2$, and WTe_2) on the SiO_2 substrate using sputtering deposition followed by solid-phase crystallization (SPC) via long-duration furnace annealing (FA) in inert ambient at low temperatures, which we refer to as 2DSPC.[24,25] The scale-up potential in area is guaranteed because stoichiometric transition metal and chalcogen sources are directly supplied from a compound sputter target, and the SPC process requires neither complex chemical reactions nor expensive crystalline substrates. 2DSPC is simple and cost-effective, involving three subsequent growth stages: nucleation, crystal growth, and coalescence, similar to the SPC of amorphous Si (α-Si).[26-28] The SPC of α-Si has been investigated for years because of its abundant applications in polycrystalline Si (poly-Si) thin-film transistors and silicon-on-insulator technology. Compared with the synthesis of poly-Si directly at high temperatures (> 600 ℃) by low-pressure CVD, the SPC poly-Si shows higher crystallinity, lower strain, and smaller surface roughness.[29]

In this paper, the promise of 2DSPC is further showcased by the successful synthesis of highly crystalline few-layer 2H-$MoTe_2$ with a monocrystalline grain size exceeding half a

centimeter. Rather than using FA, the improved 2DSPC was carried out using rapid thermal annealing (RTA) at high temperatures for preparing sparse and monocrystalline 2H-$MoTe_2$ hexagons with a size of up to several hundred μm. High annealing temperature effectively suppressed nucleation rate while promoting crystal growth. RTA prevented parasitic nucleation during the slow heating and cooling processes in FA. The large-area uniformity, atomic structure, and crystallographic orientations of the hexagonal domains were systematically characterized by Raman spectroscopy, transmission electron microscopy (TEM), and electron back-scattered diffraction (EBSD). The 2DSPC mechanism and its intriguing hexagonal domain shape were further analyzed using the classical nucleation theory (CNT) and kinetic Wulff construction (KWC) theory, respectively. Using the sparse 2H-$MoTe_2$ hexagons as seeds, the monocrystalline domains were enlarged to half a centimeter in size by using a subsequent FA at low temperatures without forming new nucleation sites. This two-step annealing (TSA) approach effectively separated the nucleation and crystal growth stages during the crystallization process, thereby promoting the formation of extremely large-grain 2H-$MoTe_2$. Improved electrical characteristics were also shown in 2H-$MoTe_2$ synthesized using TSA. The improved 2DSPC via TSA could potentially open up a new avenue for synthesizing large-area, high-crystallinity 2D layered materials in a cost-effective manner.

Results and Discussion

Preparing Sparse 2H-$MoTe_2$ Seeds by 2DSPC

In the proposed 2DSPC, α-$MoTe_2$ was first deposited onto an amorphous SiO_2 substrate by DC magnetron sputtering using a $MoTe_2$ compound target. A SiO_2 encapsulation layer was then deposited on the film. The encapsulation layer serves two important purposes during the subsequent annealing in inert ambient.[24] First, it prevents the Te element from out-diffusion at a temperature higher than the Te sublimation temperature. Second, it confines the atom migration two-dimensionally for facilitating uniform 2D lattice crystallization. The role and the composition of the encapsulation layer have been discussed in the previous publication.[24] 2DSPC is capable of

forming few-layer 2H-$MoTe_2$ with a thickness easily controlled using the sputtering time (Fig. S1). More information on sample preparation is provided in the Experimental Methods. The α-$MoTe_2$ is initially crystallized into the 1T'-phase during thermal annealing and then transformed from 1T'- to 2H-phase as the annealing time (t_a) increases.[24,25] This phase transformation process undergoes 2H-phase nucleation, lateral crystal growth, and coalescence, as shown in Fig. 1a. According to the classical nucleation theory (CNT), the grain size of the SPC film is determined by the ratio of the nucleation rate (r_n) relative to the crystal growth velocity (v_g).[30,31] Performing 2DSPC at high temperature with a sufficiently fast ramping rate (r_{ramp}) and cooling time (t_{cool}) minimizes the ratio of r_n/v_g, thus enlarging the grain size. Therefore, α-$MoTe_2$ was annealed using high-temperature, short-duration RTA to avoid excessive nucleation occurred during the slow heating and cooling processes of FA. The annealing temperature (T_a) ranging from 700 ℃ to 850 ℃ allows stable 2H-$MoTe_2$ formation using RTA for 1 min (Table S2 and Fig. S2a-c). Higher T_a (> 850 ℃) instead stabilizes the 1T'-phase[32] while lower T_a (< 700 ℃) cannot provide sufficient activation energy for 2H-$MoTe_2$ nucleation in short-duration RTA. The r_{ramp} and t_{cool} of RTA in the range we investigated in this work have a negligible influence on the 2H-$MoTe_2$ nucleation density. A higher r_{ramp} of ~55 ℃/s and a shorter t_{cool} of 20 s was chosen for minimizing the overall thermal budget. More detailed investigations on the comparison between FA and RTA and the effects of r_{ramp}, t_{cool}, and T_a on crystallizing 2H-$MoTe_2$ in RTA are shown in Fig. S2 and Fig. S3. By optimizing T_a and t_a, sparse 2H-$MoTe_2$ domains were produced with a size of hundreds of micrometers (Fig. 1b and Fig. S4). These sparse domains are used as seeds in TSA, as will be discussed later.

The domain shape and phase distribution of 2H-$MoTe_2$ after RTA treatment were examined using the optical image and Raman spectroscopy. Fig. 1b displays the morphology of 2H-$MoTe_2$ domains after RTA at 700-850 ℃ for 5 min. The optical contrast is apparent between 2H- and 1T'-$MoTe_2$ as a result of the difference in the visible absorption spectrum.[33] Note that the shape of 2H-$MoTe_2$ domains is sensitive to T_a and t_a rather than r_{ramp} and t_{cool} in RTA (Fig. S3b and Fig. S4). Similar hexagonal 2H domains could also be obtained at high T_a in FA (r_{ramp} ~1 ℃ /s and t_{cool} ~2

hr), illustrating that the shape of 2H domains is highly correlated with T_a (Fig. S2e). With the increase of T_a and t_a in RTA, the domain of 2H-$MoTe_2$ undergoes a shape transition from round to hexagonal (Fig. 1b and Fig. S4). More details on the shape transition will be discussed later. Representative Raman spectra of 2H-$MoTe_2$ and its surrounding 1T'-$MoTe_2$ are shown in Fig. 1c. 2H-$MoTe_2$ shows two prominent Raman peaks between 120 and 280 cm^{-1}, the out-of-plane A_{1g} mode at 171 cm^{-1} and in-plane E^1_{2g} mode at 234 cm^{-1}. The peak of 163 cm^{-1} (B_g mode) is the major vibrational mode of 1T'-$MoTe_2$. Both the Raman spectra of 1T' and 2H phases are similar to those reported in the literature.[32,33] The uniformity of 2H phase within the hexagonal domain was further characterized by the Raman mapping in Fig. 1d. The result shows a uniform distribution of the E^1_{2g} peak intensity, indicating the spatial homogeneity of 2H phase over the entire domain.

Monocrystallinity of 2DSPC 2H-$MoTe_2$

The atomic structure and crystallinity of hexagonal 2H-$MoTe_2$ domains after RTA was further examined using high-resolution TEM (HRTEM) and spherical aberration-corrected scanning TEM (Cs-STEM). The cross-sectional HRTEM image in Fig. 2a shows four-layer stacking of 2H-$MoTe_2$ with a thickness of 2.87 nm (or 0.71 nm per layer), which is consistent with the thickness obtained from exfoliation,[11] CVD,[34] or post-tellurization methods.[35] After removing the SiO_2 encapsulation layer, the hexagonal domains were transferred onto a copper grid for the plane-view TEM observation. Details of the transfer process are provided in the Experimental Methods. The plane-view TEM image and selected area electron diffraction (SAED) pattern illustrate that the four-layer 2H-$MoTe_2$ possesses an almost perfect hexagonal lattice with a single set of six-fold symmetric diffraction array (Fig. 2b and c). The filtered Cs-STEM high-angle annular dark-field (HAADF) image in Fig. 2d also shows the ideal hexagonal arrangement of Mo and Te atoms corresponding to the 2H phase. By contrast, 1T'-$MoTe_2$ in the surroundings of the 2H-$MoTe_2$ domain exhibited a rather disordered lattice arrangement where most regions retained amorphous after annealing (Fig. 2e and f).

To confirm the crystallinity of the hexagonal 2H-$MoTe_2$ domain, the SAED patterns of nine different locations over the entire 200-μm domain were examined (Fig. 2g and h). This approach has also been applied to verify the crystallinity of graphene[36] and MoS_2[37] over a large area. The diffraction patterns in different locations showed negligible misalignment of less than two degrees, confirming that the entire hexagonal domain is a single monocrystalline grain. The SAED patterns in the vicinity of domain edges were also characterized (Fig. S5). The diffraction patterns indicate that the 2H-$MoTe_2$ domain is with the zig-zag (ZZ) edges, as expected in the literature.[38,39] The dominant ZZ edge is due to the higher formation energies of the nucleus on a ZZ edge than on an arm-chair (AC) edge.[40] Additionally, the EBSD mapping[41,42] was also performed to inspect the distribution of crystallographic orientation (Fig. S6). The inverse pole figures along x-, y-, and z-axis (IPF-X, IPF-Y, and IPF-Z) reveal a uniform distribution, in which the orientations of 2H-$MoTe_2$ parallel to the substrate are roughly aligned with the $<\bar{1}2\bar{1}0>$- and $<01\bar{1}0>$-directions corresponding to the x- and y-axis, respectively. The results are consistent with the TEM observation, showing the hexagonal domain is dominated by the ZZ edges. In summary, both TEM/SAED patterns and EBSD mapping results confirm the high crystalline homogeneity of the RTA-annealed 2H-$MoTe_2$.

Grain Size of 2DSPC: Classical Nucleation Theory

The grain size of the 2DSPC 2H-$MoTe_2$ is further analyzed using r_n and v_g. r_n was calculated by dividing the number of 2H-$MoTe_2$ domains by the substrate area and t_a (fixed at 5 min for RTA). A representative optical image (Fig. S7) contains six 2H-$MoTe_2$ domains on a substrate area of ~1 cm^2, corresponding to r_n of ~ 1.2 $min^{-1}cm^{-2}$. Fig. 3a presents the relation between r_n and T_a in RTA. r_n increases with T_a at low temperatures but then decreases as T_a further increases. The characteristic inverted U-shape curve agrees well with the prediction of CNT.[31,35] The reduced r_n at high temperatures could be explained by the critical cluster size effect and higher stability of the 1T'-phase.[31,32] After the initial nucleation, the 2H nucleus begins to grow outward into the surrounding 1T' area via the atom rearrangements and 1T'-to-2H phase transformation. v_g

perpendicular to ZZ-plane ($v_{g,\,ZZ}$) and AC-plane ($v_{g,\,AC}$) was extracted from the distance of the extending region from a specific grain at various T_a by using a time interval of 5 min, as shown in Fig. 3b. Generally speaking, the growth process is governed by thermally-induced atomic diffusion, and v_g increases exponentially with temperature. Both $v_{g,\,ZZ}$ and $v_{g,\,AC}$ increase as T_a increases, and the mean values are around 0.3 and 0.4 μm/s at 850 °C, respectively. According to the Johnson-Mehl-Avrami-Kolmogorov equation in the 2D case,[35] the final grain size in a completely crystallized film could be estimated as ~$(v_g/r_n)^{1/3}$ (~2.5 mm at 850 °C) (for details, see Supporting Information). Theoretically, a millimeter size of monocrystalline grains could be achieved by prolonging t_a. However, the maximum t_a was limited to 5 min due to the hardware limitation of our RTA setup. Consequently, the grain size in our partially crystallized film was predominated by v_g because of the low nucleation density. The mean grain size shown in Fig. 3c increases with T_a and reaches a value of approximately 300 μm at 850 °C.

Morphological Evolution: Kinetic Wulff Construction Theory

The morphological evolution has been investigated in CVD-synthesized 2D materials, such as MoS_2[43,44] and graphene.[45,46] The KWC theory was introduced to evaluate the quasi-stationary dynamic morphology of a growing crystal by tracing the slowest v_g of a specific facet.[45,47,48] For example, the KWC theory predicts the coexistence of both ZZ and AC edges and a polygon (or circular) domain for graphene with a growth speed ratio ($v_{g,\,AC}/v_{g,\,ZZ}$) between $\sqrt{3}/2$ and $2/\sqrt{3}$; outside of this range, the edge type of graphene is dominated by either ZZ or AC, resulting in a hexagonal domain.[45] For most CVD-synthesized group-VI TMDs and graphene, the boundaries of a hexagonal domain are typically the ZZ edge due to its higher formation energy of kink nucleation.[45,46,48] More atoms are required to complete a hexagon at the ZZ edge, thereby becoming energy unfavorable and slowing down the growth speed.[45] In addition to the ZZ and AC edges, the slanted edges with an ~19° angle (refer to as S19 in ref. 48) could also be observed in circular graphene domains. The formation of such S19 edges requires lower energy than that of the AC and ZZ edges and thus could be observed before the domain eventually saturates to the ZZ edges.

Time evolution (t_a from 1 to 5 min) of the 2H-$MoTe_2$ domain (Fig. S4) demonstrates a similar transformation of domain shape from circular to hexagonal. We also characterized this transformation using two subsequent RTA processes (Fig. S8), suggesting that the hexagonal domain was transformed by eliminating S19 edges at high T_a. However, no such shape evolution was observed at low T_a (< 750 ℃). The relation between domain shape and T_a could be quantitatively explained using the KWC theory. v_g is typically expressed using the Arrhenius equation, $v_g \propto e^{\frac{-E_B}{kT}}$, where E_B is the threshold energy barrier.[47-49] Therefore, the difference of E_B between two edges (E_{ZZ}-E_{AC}) could be extracted by measuring $v_{g,\,ZZ}$ and $v_{g,\,AC}$, as shown in Fig. 3d. There are no noticeable differences between $v_{g,\,ZZ}$ and $v_{g,\,AC}$ below 750 ℃, and the isotropic growth prompts the circular domain shape. By contrast, a significant v_g difference of 0.1 μm/s exists between the AC- and ZZ-edges at 850 ℃. The hexagonal edges are restricted by the lower $v_{g,\,ZZ}$ at high T_a, resulting in a hexagon domain with the ZZ-dominated edges. The theoretical ratio of $v_{g,\,AC}$ /$v_{g,\,ZZ}$ are $2/\sqrt{3}$ and $\sqrt{3}/2$ for ZZ- and AC-dominated hexagons, respectively, by considering the geometric distance ratio of a hexagon from the center to corners and sides. The difference of E_B reaches 20 meV at higher T_a, thus favoring a ZZ-terminated hexagonal domain.

TSA-assisted 2DSPC for Extremely Large-Grain 2H-$MoTe_2$

Although 2DSPC successfully demonstrated monocrystalline 2H-$MoTe_2$ as large as 300 μm by minimizing the ratio of r_n/v_g in RTA at high T_a, two limitations require further improvement. First, the typical RTA chamber is not designed for performing high-temperature annealing with a substantial duration. Furthermore, new nucleation sites of 2H-$MoTe_2$ could be still formed during prolonged RTA at high T_a. Therefore, enlarging the grain size beyond the millimeter- or even centimeter-scale in a completely crystallized film requires novel approaches. Second, the dendrite-like nano-cracks are regularly observed in 2DSPC 2H-$MoTe_2$ annealed at high T_a regardless of the heating instrument (RTA or FA) (Fig. S9). These nano-cracks only exist inside the 2H-$MoTe_2$ domains but not the nearby 1T'-$MoTe_2$ and produce a radial pattern with significant contrast in the optical image. The cross-sectional HRTEM image reveals that these cracks are the local

discontinuity of 2H-$MoTe_2$ underneath the encapsulation layer. They could physically block carrier transport and thus degrade the device performance. More details on the nano-crack formation are provided in the Supporting Information. From our previous studies,[24,25] the 1T'-2H phase transformation is accompanied by Te migration from the Te-aggregated region located at the phase boundary between 1T'-$MoTe_2$ and 2H-$MoTe_2$. The high-annealing temperature might aggravate Te migration and induce non-negligible stress to the film.

By using the RTA-annealed monocrystalline hexagonal 2H-$MoTe_2$ domains as seeds, we propose using a second annealing step carried out in a furnace to enlarge the grain size at a relatively lower temperature for a longer duration. The condition of FA was chosen so that it only allows 2H-$MoTe_2$ growing from the preexisting monocrystalline domains without forming new nucleation sites, i.e. r_n/v_g approaching zero. This strategy, which we refer to as TSA, effectively separates the nucleation and crystal growth stages, thereby promoting the formation of large-grain 2H-$MoTe_2$. TSA was inspired by the similar technique used for crystallizing α-Si,[50,51] which not only demonstrated better device performance than those fabricated using the conventional SPC but also improved uniformity in electrical characteristics.

Herein, the process condition of the first-step RTA was selected at 850 ℃ for 5 min to reduce the nucleation density of hexagonal 2H-$MoTe_2$ domains. Although achieving low r_n is also possible at lower T_a, but significant process variation exists and compromises the reproducibility (Fig. S10). The second-step FA was performed for crystal growth at 550 ℃ for 24 hr, which is thermally insufficient to nucleate 2H phases but enough to enlarge the preexisting domains without forming nano-cracks. Fig. 4a shows the crystal growth of 2H-$MoTe_2$ domains before and after the second-step FA. The 2H-$MoTe_2$ domains only grew outward from the initial seeds and reached a size greater than 2 mm. The domain shape also transformed from hexagonal after RTA to circular after FA because of the comparable $v_{g,\,ZZ}$ and $v_{g,\,AC}$ at low temperatures. By contrast, the control sample without RTA did not produce any 2H-$MoTe_2$ domains after FA at 550 ℃. The result confirms that the activation energy for 2H-$MoTe_2$ nucleation is higher than that for 2H-$MoTe_2$

crystal growth. The substantial difference in activation energies for nucleation and crystal growth in 2H-$MoTe_2$ plays a vital role in TSA-assisted 2DSPC.

The uniformity of 2H-$MoTe_2$ synthesized using TSA was characterized by Raman spectra along the radial direction of the grain (indicated by the red arrow in Fig. 4a). Fig. 4b presents the statistics of the major Raman peak of E^1_{2g} and its corresponding full width of half maximum (FWHM). Low variation of the E^1_{2g} peak indicates the large-area uniformity of 2H-$MoTe_2$. The crystallinity of large-area 2H-$MoTe_2$ synthesized by FA and TSA was compared using the EBSD mapping. We chose an optimized FA condition[24,25]: 650 ℃ for 24 hr to compare with TSA. Note that the higher T_a is required than that used in the second-step annealing in TSA to overcome the higher activation energy for nucleation. Fig. 4c displays the EBSD color map (IPF-X) of selected areas from both samples. Various crystallographic orientations were interleaved in the FA-annealed 2H-$MoTe_2$, which indicates a high r_n /v_g ratio in one-step FA at 650 ℃. In the TSA sample, however, the IPF-X measurement exhibits a uniform color map over a large area (~1 mm^2) of the FA-grown regions. Growth of the monocrystalline crystal in FA was found to be independent of the initial shape of the 2H-$MoTe_2$ seed formed by RTA (Fig. S11). Fig. 4d displays a monocrystalline 2H-$MoTe_2$ domain with a size exceeding half a centimeter by extending t_a in FA to four days. The long t_a in FA should not be a throughput bottleneck in the semiconductor process because a batch furnace processes more than one hundred wafers at a time. TSA-assisted 2DSPC is expected to produce an even larger grain size by selectively etching away unnecessary nucleation sites or transferring only one single seed onto a new substrate.

The synthesis methods of 2H-$MoTe_2$ proposed in the literature include micromechanical exfoliation,[32] chemical vapor transport (CVT),[52,53] molecular beam epitaxy (MBE),[53] physical vapor deposition (PVD),[24,25] CVD methods,[55,56] etc. Generally speaking, there is still a lack of effective techniques for synthesizing large-grain 2H-$MoTe_2$ while controlling the thickness to a few layers. For example, MBE effectively controlled the thickness of 2H-$MoTe_2$, but the grain size was as small as tens of nanometers.[54] High-quality, large-grain 2H-$MoTe_2$ could be produced using the CVT method followed by mechanical exfoliation; however, the difficulty in thickness control

over a large area makes it impractical for applications. Some CVD methods, such as the tellurization of Mo or MoO_x films, have also been reported to successfully synthesize 2H-$MoTe_2$.[35,42] However, such growth processes were mediated by vapor transport and involved complicated chemical reactions. The phase control of $MoTe_2$ was also found highly sensitive to the precursor tuning in the CVD systems. To separately control nucleation and crystal growth for enlarging the grain size remains challenging in CVD. Recently, X. Xu et al. have presented a promising method for directly synthesizing large-scale 2H-$MoTe_2$ on insulating substrates by seed crystal implantation.[61] Tellurization of 1T'-$MoTe_2$ was carried out using a single 2H-$MoTe_2$ seed and oxide encapsulation, which prevents undesired nucleation and ensures monocrystalline growth. The seed-induced in-plane 2D growth may completely cover a 1-inch wafer with high uniformity. However, the seed/1T'-$MoTe_2$ interface properties, such as surface roughness and film continuity, play an important role in the phase transition for few-layer $MoTe_2$.[61] More efforts for surface optimization are required to reduce the film thickness even further. By comparison, our proposed TSA-assisted 2DSPC is a relatively simple, controllable, and reproducible technique for synthesizing large-grain $MoTe_2$. Fig. 4e compares the grain size from literatures[35, 54-60] and our work for few-layer $MoTe_2$. Our 2DSPC presents one of the most promising routes for synthesizing future centimeter-scale monocrystalline $MoTe_2$ and potentially a wider variety of 2D materials.[24]

Electrical Characterization of TSA-assisted 2DSPC 2H-$MoTe_2$

Fig. 5a illustrates the representative transfer characteristics (drain current (I_D) versus gate voltage (V_G)) of back-gated 2H-$MoTe_2$ transistors where channel materials were synthesized using FA and TSA, respectively. In the case of TSA, 2H-$MoTe_2$ transistors in a millimeter-scale area with the ZZ- or AC channel orientation are defined along the edges and corners of the hexagonal seed in the center of the grain (Fig. S12 and the inset in Fig. 5a). As for FA, the channel direction is along arbitrary crystal orientations because of its polycrystalline nature. The device channel length/width (L/W) is 10 μm/24 μm, and Pd (30 nm) was deposited by electron-beam evaporation as the source/drain (S/D) contact. Both FA- and TSA-synthesized devices exhibited p-type

conduction characteristics, similar to those reported in the literature.[62,63] The high metal work function of Pd and partial oxidation of the $MoTe_2$ film are plausible explanations for p-type conduction.[25] Fig. 5a shows comparable electrical performance for the $MoTe_2$ transistors with the ZZ and AC channel orientations. A. Rawat et al. comprehensively analyzed the carrier mobility of various group-VI TMDs by considering three types of mobility models.[64] All the group-VI TMDs show small deviations of effective mass, acoustic phonon-limited deformation potential, and elastic modulus in the ZZ and AC directions, thereby reducing the anisotropy of carrier mobility and device performance. Fig. 5b-d compare the statistical data of electrical properties (I_{ON}, on/off ratio, and mobility) extracted from transistors based on FA and TSA. The field-effect hole mobility (μ_h) in the linear region was extracted using $\mu_h = (dI_D/dV_G)(L/W)(1/V_D C_G)$ at $V_D = -1$ V, where V_D and C_G represent the drain voltage and gate capacitance per unit area, respectively. The results indicate that the FA-synthesized device is generally inferior to those obtained using TSA. According to our previous EBSD analysis (Fig. 4c), the grain boundary scattering in the FA-synthesized 2H-$MoTe_2$ could be a plausible explanation for the degraded electrical performance. T. H. Ly et al. investigated the carrier transport at grain boundaries of MoS_2 and showed the electrostatic potential barrier across domains deteriorated the mobility and I_{ON} of MoS_2 devices.[65] Similar results were also observed elsewhere,[66,67] highlighting the importance of high crystallinity in 2D-material synthesis.

Conclusions

In summary, we present a simple yet effective 2DSPC technique for synthesizing 2H-$MoTe_2$ with a monocrystalline grain size up to half a centimeter. The TSA strategy allows the nucleation and crystal growth of 2DSPC to be separately controlled by RTA and FA due to their significant difference in activation energy. The temperature-dependent evolution of domain size and morphology of 2H-$MoTe_2$ could be explained using CNT and KWC, respectively. Because the sputtering and the thermal annealing in inert gas are easily scaled up in semiconductor processes, 2DSPC is a highly promising synthesis route for integrating large-area, high-quality 2D

TMDs in the advanced semiconductor platform. Future research should address the strategy to further enlarge the grain size and position the grains in well-defined locations. Applying 2DSPC for synthesizing a wider variety of 2D materials with extremely large grain sizes should also be explored.

Experimental Methods

2DSPC $MoTe_2$ Synthesis using TSA

Continuous α-$MoTe_2$ films were deposited onto a Si substrate with 300 nm-thick SiO_2 by DC magnetron sputtering using a compound $MoTe_2$ target for 40 s at a substrate temperature of 200 ℃. The as-deposited α-$MoTe_2$ was immediately capped with a 50 nm-thick electron-beam evaporated SiO_2 and a 50 nm-thick plasma-enhanced CVD SiO_2. This bilayer SiO_2 encapsulation plays a vital role in the subsequent crystallization process to prevent Te from out-diffusion and facilitate the formation of 2D layered $MoTe_2$. The SiO_2/α-$MoTe_2$/SiO_2 samples were then loaded into the RTA chamber (Allwin AW 810M, Accuthermo Technology Corp.) with a fixed r_{ramp} of 55 ℃/s and t_{cool} of 20 s at 700-850 ℃ for 5 min to promote the 2H-$MoTe_2$ nucleation. The second-step FA was performed at 550 ℃ for 24 hr with r_{ramp} of 1 ℃ /s and t_{cool} of 1.5 hr to facilitate the crystal growth of 2H-$MoTe_2$.

Physical Characterization of $MoTe_2$

The optical properties of $MoTe_2$ were characterized by Raman spectroscopy using a WITec Alpha 300RA system with a 532-nm Nd: YAG laser as the excitation source. The Raman spectrum was measured in a backscattering configuration using a 100× objective lens with 1200 grooves/mm gratings. A laser power of 15 μW was chosen to avoid substrate heating. The step size for Raman mapping was 4.5 μm with scanning points of 64×64. For the sample preparation of EBSD (JEOL JSM-7800F PRIME + EBSD NordlysMax3, the acceleration voltage is at 20 kV), the SiO_2/$MoTe_2$/SiO_2 samples were cut into a size of 1cm × 1cm, and the SiO_2 encapsulation layer on the 2DSPC 2H-$MoTe_2$ films were etched using high-density plasma reactive ion etching (HDP-

RIE). The step size and grid of EBSD mapping for 2H-$MoTe_2$ annealed by RTA and TSA were 2.5 μm & 170×145 and 5 μm & 234×175, respectively. To prepare the sample for plane-view HRTEM (Tecnai G2 F20), 90 nm-thick SiO_2 on the 2DSPC 2H-$MoTe_2$ was etched by CHF_3 and Ar using HDP-RIE. The sample was then immersed in a diluted hydrofluoric (DHF) solution (1.2%) at room temperature to remove the remained SiO_2 encapsulation and detach the film from the substrate. Subsequently, the film was transferred onto a lacey carbon film on a mesh copper grid.

Fabrication of Back-Gated $MoTe_2$ Transistors

The SiO_2 encapsulation layer of $MoTe_2$ at the S/D regions was etched similar to that used for preparing the HRTEM samples. The encapsulation layer on top of the channel remains intact. The S/D regions were defined using photolithography, and the remained SiO_2 on top of S/D regions was removed using DHF etching. A 30 nm-thick Pd was then deposited using electron-beam evaporation followed by a lift-off process in acetone. The active channel region was then patterned by photolithography and plasma dry etching using CHF_3 and Ar. The electrical characteristics of back-gated $MoTe_2$ transistors were measured at room temperature using a B1500A semiconductor device parameter analyzer.

Author Contributions

C.-P.L., H.-H.H and T.-H.H generated the idea and designed the work. C.-P.L., H.-H.H, and J.-H.H prepared the sample and measured the device. C.-P.L., Y.-W.K, and C.-T.W performed physical analysis. C.-P.L., Y.-J.L., C.-C.C., Y.-W.L., W.-H.C., L.-J.L., and T.-H.H. analyzed the experimental results. C.-P.L. and T.-H.H. prepared the manuscript.

Conflicts of interest

There are no conflicts of interest to declare.

Acknowledgments:

This work was supported by the Ministry of Science and Technology, Taiwan under grant: 106-2221-E-009-145-MY3 and 107-2633-E-009-003 (Research of Excellence program), Taiwan Semiconductor Research Institute, the Asian Office of Aerospace Research and Development (AOARD), the Office of Naval Research Global (ONRG), and AU Optronics.

References

1 N. K. Nepal, L. Yu, Q. Yan and A. Ruzsinszky, *Phys. Rev. Materials*, 2019, **3**, 073601.

2 D. Wickramaratne, F. Zahid and R. K. Lake, *J. Chem. Phys*., 2014, **140**, 124710.

3 J. Kang, S. Tongay, J. Zhou, J. Li and J. Wu, *Appl. Phys. Lett.*, 2013, **102**, 012111.

4 A. Splendiani, L. Sun, Y. Zhang, T. Li, J. Kim, C. –Y. Chim, G. Galli and F. Wang, *Nano Lett.*, 2010, **10**, 1271-1275.

5 Z. Yu, Z. –Y. Ong, S. Li, J. –B. Xu, G. Zhang, Y. –W. Zhang, Y. Shi and X. Wang, *Adv. Funct. Mater.*, 2017, **27**, 1604093.

6 M. Hosseini, M. Elahi, M. Pourfath and D. Esseni, *IEEE Trans. Electron Devices*, 2015, **62**, 3192-3198.

7 Y. Liu, X. Duan, Y. Huang and X. Duan, *Chem. Soc. Rev.*, 2018, **47**, 6388-6409.

8 J. R. D. Retamal, D. Periyanagounder, J. –J. Ke, M. –L. Tsai and J. –H. He, *Chem. Sci.*, 2018, **9**, 7727-7745.

9 B. Radisavljevic, A. Radenovic, J. Brivio, V. Giacometti and A. Kis, *Nat. Nanotechnol.*, 2011, **6**, 147-150.

10 D. Akinwande, C. Huyghebaert, C. –H. Wang, M. I. Serna, S. Goossens, L. –J. Li, H. –S. P. Wong and F. H. L. Koppens, *Nature*, 2019, **573**, 507-518.

11 C. Ruppert, O. B. Aslan and T. F. Heinz, *Nano Lett.*, 2014, **14**, 6231-6236.

12 W. Zhang, Z. Huang, W. Zhang and Y. Li, *Nano Res.*, 2014, **7**, 1731-1737.

13 Th. Böker, R. Severin, A. Müller, C. Janowitz, R. Manzke, D. Voβ, P. Krüger, A. Mazur and J. Pollmann, *Phy. Rev. B*, 2011, **64**, 235305.

14 K. –A. N. Duerloo, Y. Li and E. J. Reed, *Nat. Commun.*, 2014, **5**, 4214.

15 J. Park, K. –H. Xue, M. Mouis, F. Triozon and A. Cresti, *Phys. Rev. B*, 2019, **100**, 235403.

16 A. M. van der Zande, P. Y. Huang, D. A. Chenet, T. C. Berkelbach, Y. You, G. –H. Lee, T. F. Heinz, D. R. Reichman, D. A. Muller and J. C. Hone, *Nat. Mater.*, 2013, **12**, 554-561.

17 A. Zavabeti, A. Jannat, L. Zhong, A. A. Haidry, Z. Yao and J. Z. Ou, *Nano-Micro Lett.*, 2020, **12**, 66.

18 L. Tao, K. Chen, Z. Chen, W. Chen, X. Gui, H. Chen, X. Li and J. –B. Xu, *ACS Appl. Mater. Interfaces*, 2017, **9**, 12073-12081.

19 Z. Zhang, P. Chen, X. Yang, Y. Liu, H. Ma, J. Li, B. Zhao, J. Luo, X. Duan and X. Duan, *Natl. Sci. Rev.*, 2020, **7**, 737-744.

20 J. Chen, X. Zhao, S. J. R. Tan, H. Xu, B. Wu, B. Liu, D. Fu, W. Fu, D. Geng, Y. Liu, W. Liu, W. Tang, L. Li, W. Zhou, T. C. Sum and K. P. Loh, *J. Am. Chem. Soc.*, 2017, **139**, 1073-1076.

21 S. –Y. Kim, J. Kwak, C. V. Ciobanu and S. –Y. Kwon, *Adv. Mater.*, 2019, **31**, 1804939.

22 H. Ye, J. Zhou, D. Er, C. C. Price, Z. Yu, Y. Liu, J. Lowengrub, J. Lou, Z. Liu and V. B. Shenoy, *ACS Nano*, 2017, **11**, 12780-12788.

23 M. Chubarov, T. H. Choudhury, D. R. Hickey, S. Bachu, T. Zhang, A. Sebastian, A. Bansal, H. Zhu, N. Trainor, S. Das, M. Terrones, N. Alem and J. M. Redwing, *ACS Nano*, 2021, **15**, 2532-2541.

24 J. –H. Huang, K. –Y. Deng, P. –S. Liu, C. –T. Wu, C. –T. Chou, W. –H. Chang, Y. –J. Lee and T. –H. Hou, *Adv. Mater. Interfaces,* 2017, **4**, 1700157.

25 J. –H. Huang, H. –H. Hsu, D. Wang, W. –T. Lin, C. –C. Cheng, Y. –J. Lee and T. –H. Hou, *Sci. Rep.*, 2019, **9**, 8810.

26 Lee, D. N.; Lee, S. B. Solid-Phase Crystallization of Amorphous Silicon Films. In *Advanced Topics in Crystallization*; Mastai, Y., Ed.; InTechOpen: London, **2015**; Ch. 9.

27 Y. Masaki, P. G. LeComber and A. G. Fitzgerald, *J. Appl. Phys.*, 1993, **74**, 129-134.

28 T. Matsuyama, N. Terada, T. Baba, T. Sawada, S. Tsuge, K. Wakisaka and S. Tsuda, *J. Non-Cryst. Solids*, 1996, **198-200**, 940-944.

29 G. Harbeke, L. Krausbauer, E. F. Steigmeier, A. E. Widmer, H. F. Kappert and G. Neugebauer, *J. Electrochem. Soc.*, 1984, **131**, 675-682.

30 J. Zhou, J. Lin, X. Huang, Y. Zhou, Y. Chen, J. Xia, H. Wang, Y. Xie, H. Yu, J. Lei, D. Wu, F. Liu, Q. Fu, Q. Zeng, C. –H. Hsu, C. Yang, L. Lu, T. Yu, Z. Shen, H. Lin, B. I. Yakobson, Q. Liu, K. Suenaga, G. Liu and Z. Liu, *Nature*, 2018, **556**, 355-359.

31 Subramanian, V. Control of Nucleation and Grain Growth in Solid-Phase Crystallized Silicon for High-Performance Thin Film Transistors.; Stanford University, **1998**.

32 D. H. Keum, S. Cho, J. H. Kim, D. –H. Choe, H. –J. Sung, M. Kan, H. Kang, J. –Y. Hwang, S. W. Kim, H. Yang, K. J. Chang and Y. H. Lee, *Nat. Phys.*, 2015, **11**, 482-486.

33 Y. Yoo, Z. P. DeGregorio, Y. Su, S. J. Koester and J. E. Johns, *Adv. Mater.*, 2017, **29**, 1605461.

34 L. Meng, C. Xu, H. Li, X. Wang and X. Yan, *Chem. Phys. Lett.*, 2019, **728**, 156-159.

35 X. Xu, S. Chen, S. Liu, X. Cheng, W. Xu, P. Li, Y. Wan, S. Yang, W. Gong, K. Yuan, P. Gao, Y. Ye and L. Dai, *J. Am. Chem. Soc.*, 2019, **141**, 2128-2134.

36 V. Miseikis, F. Bianco, J. David, M. Gemmi, V. Pellegrini, M. Romagnoli and C. Coletti, *2D Mater.*, 2017, **4**, 021004.

37 W. Chen, J. Zhao, J. Zhang, L. Gu, Z. Yang, X. Li, H. Yu, X. Zhu, R. Yang, D. Shi, X. Lin, J. Guo, X. Bai and G. Zhang, *J. Am. Chem. Soc.*, 2015, **137**, 15632-15635.

38 Q. Yu, L. A. Jauregui, W. Wu, R. Colby, J. Tian, Z. Su, H. Cao, Z. Liu, D. Pandey, D. Wei, T. F. Chung, P. Peng, N. P. Guisinger, E. A. Stach, J. Bao, S. –S. Pei and Y. P. Chen, *Nat. Mater.*, 2011, **10**, 443-449.

39 J. H. Sung, H. Heo, S. Si, Y. H. Kim, H. R. Noh, K. Song, J. Kim, C. –S. Lee, S. –Y. Seo, D. –H. Kim, H. K. Kim, H. W. Yeom, T. –H. Kim, S. –Y. Choi, J. S. Kim and M. –H. Jo, *Nat. Nanotechnol.*, 2017, **12**, 1064-1070.

40 X. Zhang, J. Xin and F. Ding, *Nanoscale*, 2013, **5**, 2556-2569.

41 S. Kim, A. Konar, W. –S. Hwang, J. H. Lee, J. Lee, J. Yang, C. Jung, H. Kim, J. –B. Yoo, J. –Y. Choi, Y. W. Jin, S. Y. Lee, D. Jena, W. Choi and K. Kim, *Nat. Commun.*, 2012, **3**, 1011.

42 X. Xu, S. Liu, B. Han, Y. Han, K. Yuan, W. Xu, X. Yao, P. Li, S. Yang, W. Gong, D. A. Muller, P. Gao, Y. Ye and L. Dai, *Nano Lett.*, 2019, **19**, 6845-6852.

43 W. Zhao and F. Ding, *Nanoscale*, 2017, **9**, 2301-2309.

44 A. G. Rajan, J. H. Warner, D. Blankschtein and M. S. Strano, *ACS Nano*, 2016, **10**, 4330-4344.

45 I. V. Vlassiouk, Y. Stehle, P. R. Pudasaini, R. R. Unocic, P. D. Rack, A. P. Baddorf, I. N. Ivanov, N. V. Lavrik, F. List, N. Gupta, K. V. Bets, B. I. Yakobson and S. N. Smirnov, *Nat. Mater.*, 2018, **17**, 318-322.

46 J. Dong, L. Zhang and F. Ding, *Adv. Mater.*, 2019, **31**, 1801583.

47 V. I. Artyukhov, Y. Liu and B. I. Yakobson, *PNAS*, 2012, **109**, 15136-15140.

48 H. Shu, X. Chen, X. Tao and F. Ding, *ACS Nano*, 2012, **6**, 3243-3250.

49 T. Ma, W. Ren, X. Zhang, Z. Liu, Y. Gao, L. –C. Yin, X. –L. Ma, F. Ding and H. –M. Cheng, *PNAS*, 2013, **110**, 20386-20391.

50 C. –L. Fan, M. –C. Chen and Y. Chang, *J. Electrochem. Soc.*, 2003, **150**, H178.

51 E. Korin, R. Reif and B. Mikic, *Thin Solid Films*, 1988, **167**, 101-106.

52 K. DiCamillo, S. Krylyuk, W. Shi, A. Davydov and M. Paranjape, *IEEE Trans. Nanotechnol.*, 2019, **18**, 144-148.

53 Y. –F. Lin, Y. Xu, S. –T. Wang, S. –L. Li, M. Yamamoto, A. Aparecido-Ferreia, W. Li, H. Sun, S. Nakaharai, W. –B. Jian, K. Ueno and K. Tsukagoshi, *Adv. Mater.*, 2014, **26**, 3263-3269.

54 S. Vishwanath, A. Sundar, X. Liu, A. Azcatl, E. Lochocki, A. R. Woll, S. Rouvimov, W. S. Hwang, N. Lu, X. Peng, H. –H. Lien, J. Weisenberger, S. McDonnell, M. J. Kim, M. Dobrowolska, J. K. Furdyna, K. Shen, R. M. Wallace, D. Jena and H. G. Xing, *J. Cryst. Growth*, 2018, **482**, 61-69.

55 L. Zhou, K. Xu, A. Zubair, A. D. Liao, W. Fang, F. Ouyang, Y. –H. Lee, K. Ueno, R. Saito, T. Palacios, J. Kong and M. S. Dresselhaus, *J. Am. Chem. Soc.*, 2015, **137**, 11892-11895.

56 A. T. Hoang, S. M. Shinde, A. K. Katiyar, K. P. Dhakal, X. Chen, H. Kim, S. W. Lee, Z. Lee and J. –H. Ahn, *Nanoscale*, 2018, **10**, 21978-21984.

57 T. Kim, H. Park, D. Joung, D. Kim, R. Lee, C. H. Shin, M. Diware, W. Chegal, S. H. Jeong, J. C. Shin and J. Park, *Adv. Mater. Interfaces*, 2018, **5**, 1800439.

58 Q. He, P. Li, Z. Wu, B. Yuan, Z. Luo, W. Yang, J. Liu, G. Cao, W. Zhang, Y. Shen, P. Zhang, S. Liu, G. Shao and Z. Yao, *Adv. Mater.*, 2019, **31**, 1901578.

59 Y. J. Park, A. K. Katiyar, A. T. Hoang and J. –H. Ahn, *Small*, 2019, **15**, 1901772.

60 X. Zhu, A. Li, D. Wu, P. Zhu, H. Xiang, S. Liu, J. Sun, F. Ouyang, Y. Zhou and X. Xiong, *J. Mater. Chem. C*, 2019, **7**, 10598-10604.

61 X. Xu, Y. Pan, S. Liu, B. Han, P. Gu, S. Li, W. Xu, Y. Peng, Z. Han, J. Chen, P. Gao, Y. Ye, *Science*, 2021, **372**, 195-200.

62 J. Liu, Y. Wang, X. Xiao, K. Zhang, N. Guo, Y. Jia, S. Zhou, Y. Wu, Q. Li and L. Xiao, *Nanoscale Res. Lett.*, 2018, **13**, 291.

63 D. Qu, X. Liu, M. Huang, C. Lee, F. Ahmed, H. Kim, R. S. Ruoff, J. Hone and W. J. Yoo, *Adv. Mater.*, 2017, **29**, 1606433.

64 A. Rawat, N. Jena, Dimple and A. D. Sarkar, *J. Mater. Chem. A*, 2018, **6**, 8693-8704.

65 T. H. Ly, D. J. Perello, J. Zhao, Q. Deng, H. Kim, G. H. Han, S. H. Chae, H. Y. Jeong and Y. H. Lee, *Nat. Commun.*, 2016, **7**, 10426.

66 S. Najmaei, M. Amani, M. L. Chin, Z. Liu, A. G. Birdwell, T. P. O'Regan, P. M. Ajayan, M. Dubey and J. Lou, *ACS Nano*, 2014, **8**, 7930-7937.

67 J. Zhang, H. Yu, W. Chen, X. Tian, D. Liu, M. Cheng, G. Xie, W. Yang, R. Yang, X. Bai, D. Shi and G. Zhang, *ACS Nano*, 2014, **8**, 6024-6030.

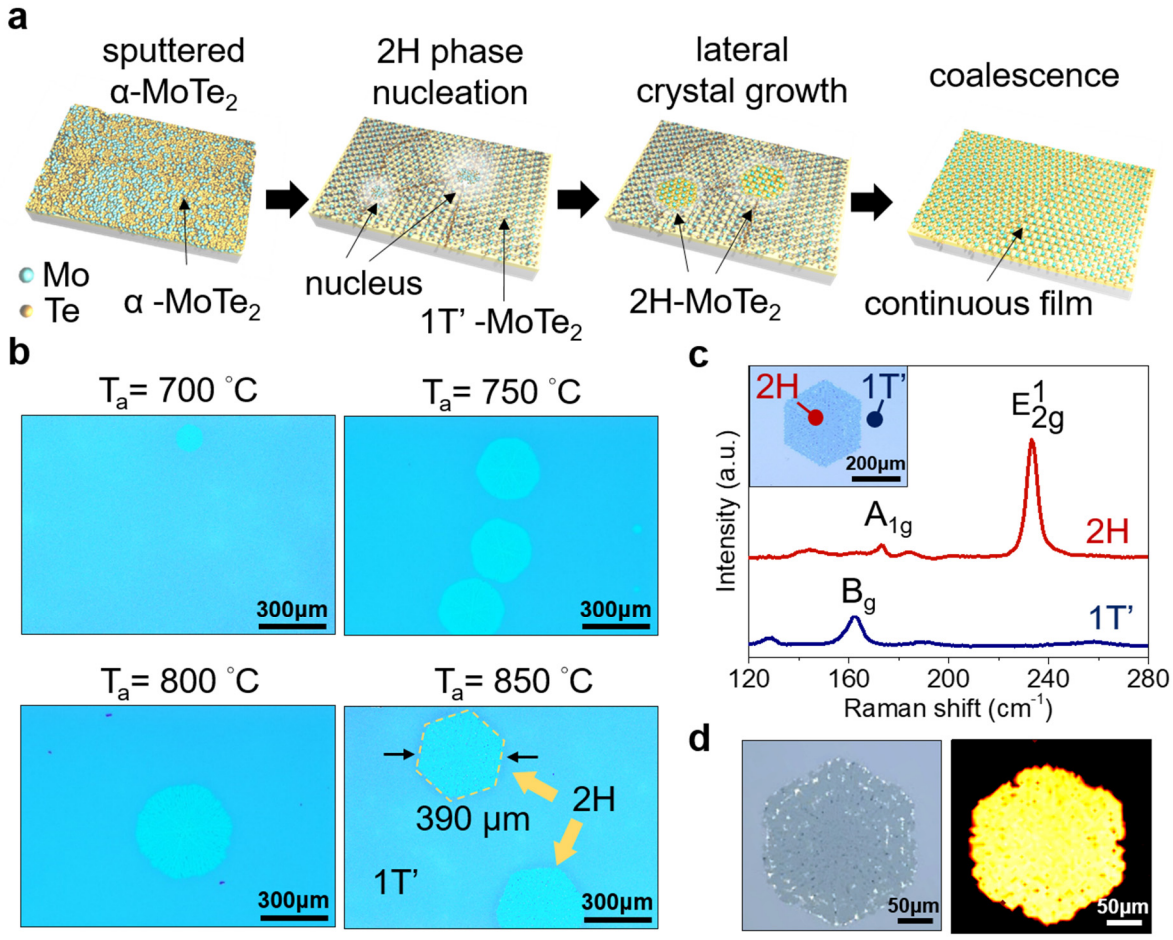

Fig. 1 2DSPC strategy for 2D layered structure synthesis. (a) Schematic illustration of 2DSPC process undergoing α-$MoTe_2$ deposition, 2H-phase nucleation, lateral crystal growth, and coalescence. (b) Optical image of 2H-$MoTe_2$ domains after RTA at 700-850 ℃ for 5 min. 2H-$MoTe_2$, as indicated by the yellow arrows, could be distinguished by the color contrast from the surrounding 1T'-$MoTe_2$. The morphology of 2H-$MoTe_2$ domains varied from circular to hexagonal as T_a increased. The domain of hexagonal 2H-$MoTe_2$ reached 390 μm at T_a= 850 ℃. (c) Representative Raman spectra of 2H-$MoTe_2$ and its surrounding 1T'-$MoTe_2$ showing the major vibrational modes of 171 (A_{1g}) and 234 (E^1_{2g}), and 163 cm^{-1} (B_g), respectively. The inset shows the hexagonal 2H-$MoTe_2$ domain annealed at T_a= 850 ℃ for 5 min. (d) Raman mapping of the hexagonal 2H-$MoTe_2$ domain characterized using the E^1_{2g} peak and its corresponding optical image.

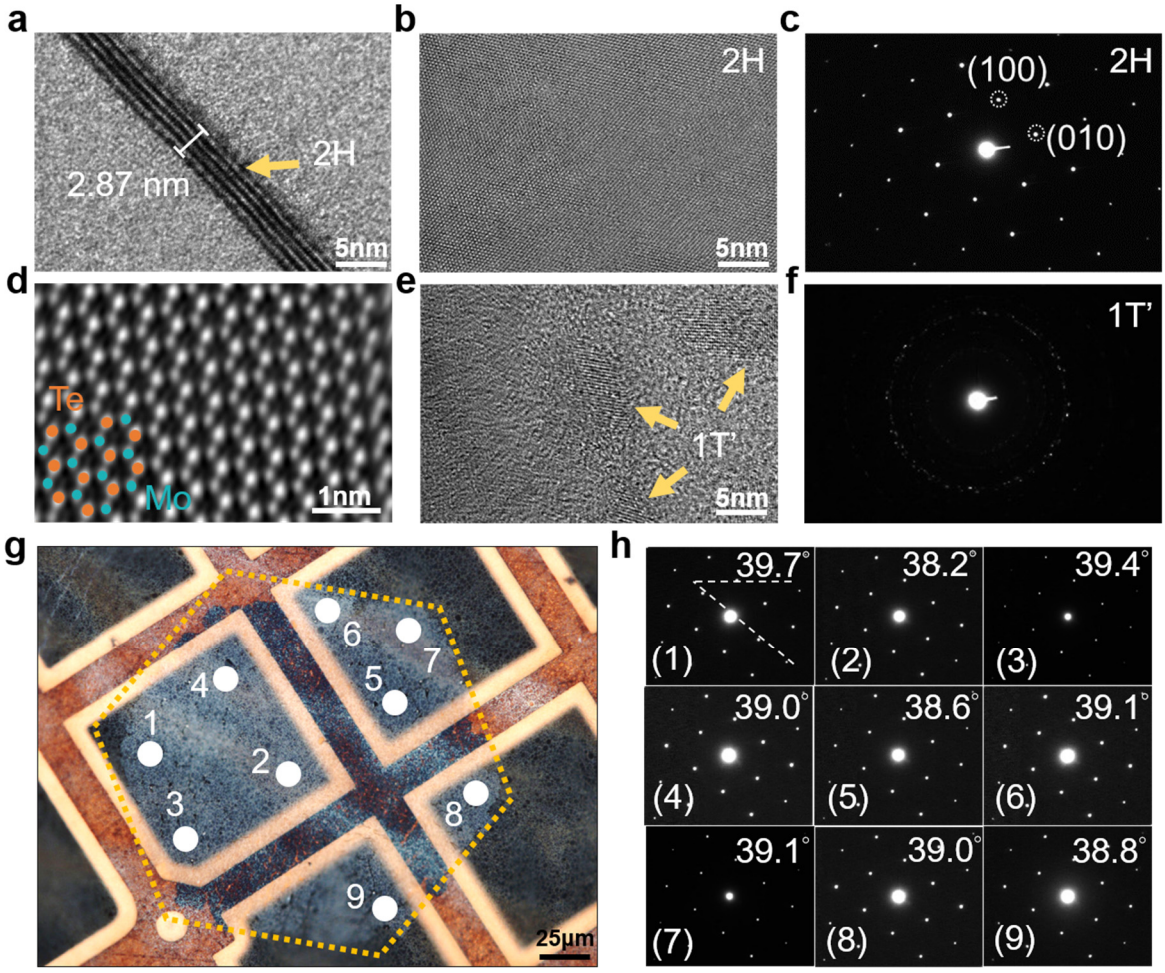

Fig. 2 Atomic structures of hexagonal 2H-$MoTe_2$ after RTA at 850 ℃ for 5 min. (a) Cross-sectional HRTEM image of 2H-$MoTe_2$, revealing a four-layer stacking structure with approximately 0.7 nm for each layer. (b) Plane-view HRTEM image of 2H-$MoTe_2$ and (c) its corresponding SAED pattern. (d) Cs-STEM image of 2H-$MoTe_2$ shows a perfect hexagonal arrangement. The bright and dark atoms correspond to Te and Mo, respectively. € Plane-view HRTEM image of 1T'-$MoTe_2$ and (f) its corresponding SAED pattern, displaying rather disordered lattice arrangement after RTA. (g) Optical image of a hexagonal 2H-$MoTe_2$ domain transferred onto a lacey carbon film on a mesh copper grid. (h) SAED patterns of 2H-$MoTe_2$ across the entire domain, where the panel 1-9 corresponds to the nine points labeled in (g). Negligible misalignment of less than two degrees confirms monocrystallinity of the hexagonal 2H-$MoTe_2$ domain.

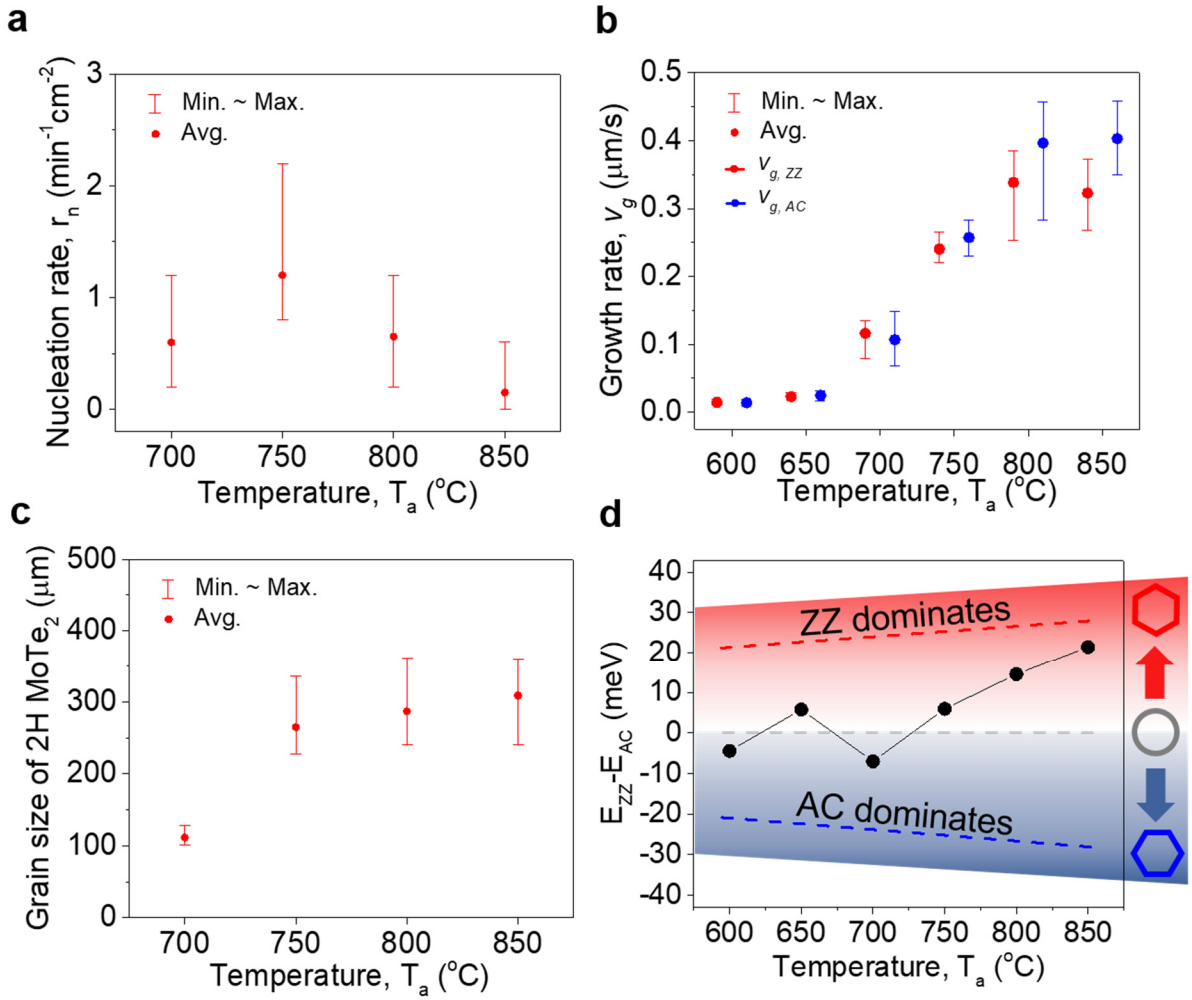

Fig. 3 Kinetic properties along ZZ and AC edges at various T_a. Competing kinetics of (a) r_n and (b) orientation-dependent v_g of 2H-$MoTe_2$ after RTA at various T_a for 5 min. (c) Statistics of 2H-$MoTe_2$ grain size as a function of T_a. The grain size increased with T_a and was limited by v_g due to the low r_n. (d) E_B difference between ZZ- and AC-edges (E_{ZZ}-E_{AC}) extracted using $v_g \propto e^{\frac{-E_B}{kT}}$. The upper and lower bounds of E_{ZZ}-E_{AC} shown in the figure correspond to the ideal ratio of $v_{g,\,ZZ}/v_{g,\,AC}$ for forming hexagonal domains with ZZ- and AC-dominated edges, respectively. By contrast, the zero E_B difference results in isotropic circular domains.

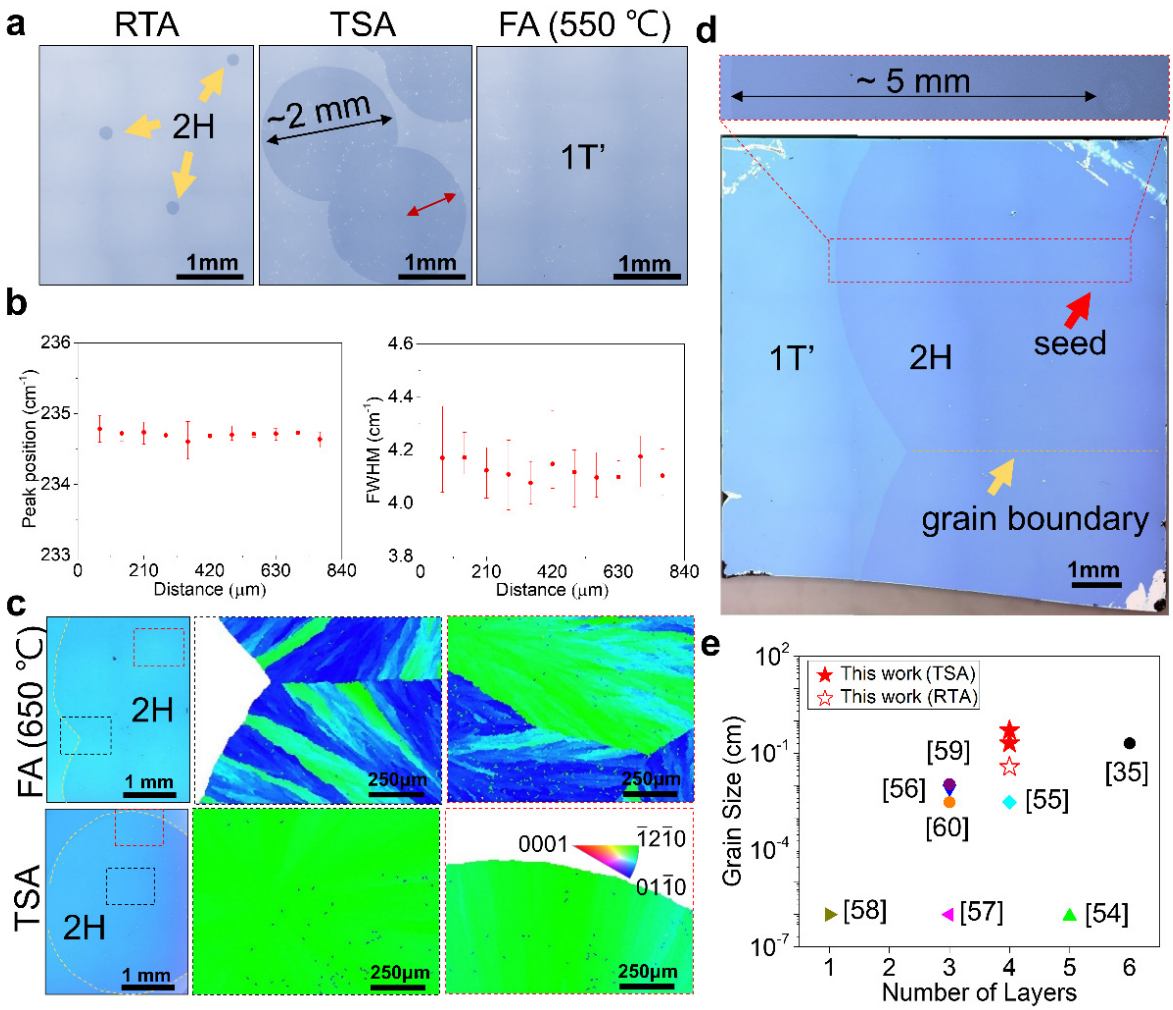

Fig. 4 Large grain size of 2H-$MoTe_2$ synthesized via TSA strategy. (a) Optical image of 2H-$MoTe_2$ domains after RTA, TSA, and FA (w/o RTA). 2H-$MoTe_2$ only grew outward from the initial seed regions during the low-temperature FA in TSA. Such low T_a (550 °C) in FA is insufficient for promoting 2H-$MoTe_2$ nucleation in the FA sample (w/o RTA). (b) Statistics of the Raman peaks of E^1_{2g} and the corresponding FWHM along the radial direction of the single domain (red arrow shown in (a). (c) EBSD color maps (IPF-X) of selected areas in FA and TSA samples. The yellow dash lines in the optical images indicate the phase boundary of 1T' and 2H domains while the black and red dash frames correspond to the regions of EBSD color maps shown on the right. (d) Optical image of a large-grain 2H-$MoTe_2$ with a size larger than 5 mm. (e) Comparison on grain sizes of few-layer 2H-$MoTe_2$ reported in the literature and this work.

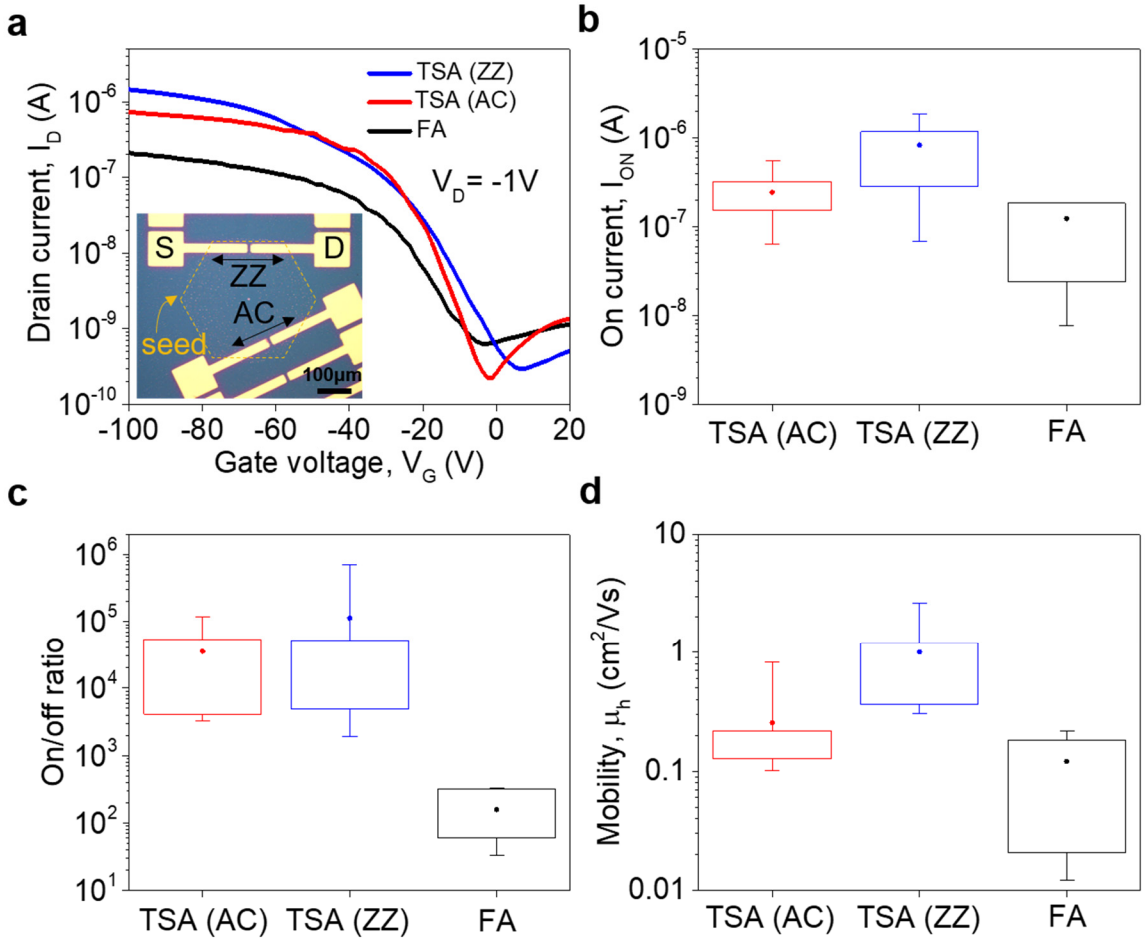

Fig. 5 Electrical properties of back-gated 2H-$MoTe_2$ transistors where channel materials were synthesized by FA and TSA. (a) Representative I_D-V_G transfer characteristics of $MoTe_2$ transistors at V_D= -1 V. The inset shows the device structures on the TSA sample where the channel direction is along either ZZ or AC orientation. Statistics of electrical properties including (b) I_{ON}, (c) on/off ratio, and (d) μ_h. The $MoTe_2$ synthesized through TSA exhibits superior device performance compared with those obtained by FA, which is attributed to the less grain boundary scattering as a result of larger granularity of 2H-$MoTe_2$. 2H-$MoTe_2$ transistors synthesized by TSA show comparable performance along the ZZ- or AC channel orientation.